Optimal Time-Step for Coupled CFD-DEM Model in Sand Production

Daniyar Kazidenov, Sagyn Omirbekov, and Yerlan Amanbek(✉)

Department of Mathematics, School of Sciences and Humanities Nazarbayev University, Kabanbay batyr 53, Astana, Kazakhstan
{daniyar.kazidenov,sagyn.omirbekov,yerlan.amanbek}@nu.edu.kz

Abstract. The coupled Computational Fluid Dynamics and Discrete Element Method (CFD-DEM) is a useful tool for modeling the dynamics of sand production that occurs in oil and gas reservoirs. To perform accurate, physically relevant and efficient calculations, the optimal size of the simulation time-step should be selected. In this study, we investigate the selection of an appropriate time-step interval between CFD and DEM models in sand production simulations. The CPU time, speedup and root mean squared relative error of the obtained results are examined to compare the sand production phenomenon at different coupling numbers. Most of the results including the final sand production rate, bond number and bond ratio indicate that the simulations with coupling numbers of $N = 10$ and $N = 100$ produce more accurate results. Moreover, these outcomes demonstrate significant improvements in terms of acceleration of the modeling process.

Keywords: Time-step · Sand production · CFD-DEM coupling

1 Introduction

Sand production is the source of many issues in the oil industry, and it has a negative impact on well completion. Plugging of lines during the perforations or production operations, wellbore instability, or the damage of a horizontal well in poorly consolidated formations tends to have environmental effects that may have additional remedial and clean-up operational costs. Moreover, it may impact the erosion of pipelines and surface facilities, which are a few issues due to sand production. Sanding prevention in wells through mechanical means is expensive and results in low output and injectivity. As a result, sand production management and modeling should be implemented early before well completions to save money [27].

Modeling the sand production process is challenging because the characteristics of fluids and sand particles should be thoroughly assessed, including particle-particle, particle-fluid, and particle-wall interactions. Recently, coupling the Computational Fluid Dynamics (CFD) and the Discrete Element Method

O. Gervasi et al. (Eds.): ICCSA 2023 Workshops, LNCS 14106, pp. 116–130, 2023.
https://doi.org/10.1007/978-3-031-37111-0_9

(DEM) system has been adopted as a promising modeling approach for particle-fluid flow problems commonly used to describe sand production phenomena [14,19].

The CFD-DEM combines the Eulerian-Lagrangian technique for modeling fluid-particle systems [24]. The Discrete Element Method (DEM) [7], which uses Newton's law to trace the movement and position of individual particles, is employed to calculate the solid phase. The Computational Fluid Dynamics (CFD) [25] models the fluid phase by solving the locally averaged Navier-Stokes equations. In DEM, the equations of motions are solved by explicit numerical integration schemes.

Several numerical coupling schemes are proposed to simulate the particle-fluid interactions. The coupling system is commonly classified into three types: resolved [23], unresolved, and semi-resolved, based on CFD mesh resolution and particle sizes. The CFD mesh resolution is much larger than the particle size in the unresolved coupled system. In comparison, the resolved case is suitable when the CFD mesh resolution is much smaller than the particle size and requires the moving immersed boundary (MIB) or immersed boundary method (IBM) to calculate interphase force. The semi-resolved CFD-DEM coupling is used when the particle size is close to the CFD mesh resolution. The interphase force calculation is determined based on the porosity calculation algorithm [26].

The unresolved approach requires few computational grids; thereby, computational efficiency is higher than resolved and semi-resolved methods and doesn't need integration along the grain boundary. However, one should note that the interphase force accuracy of the unresolved coupling method is lower than semi-resolved and resolved coupling techniques [2].

The correlation between the time-steps of DEM and CFD coupling is essential since the time-step size determines the stability of the numerical schemes. A relatively minor time-step results in precise outcomes, while more significant time-steps increase errors by resulting inaccurate results. Nevertheless, one should note that the simulation time is growing by decreasing the time-step. Therefore, the most favorable time-step to perform accurate and stable simulations should be selected.

This study is extension of the research on the sand production process in the shallow and poorly consolidated formations of the Ustyurt-Buzachi sedimentary basin of Kazakhstani oilfields, located between the Caspian Sea and the Aral Sea [13]. Sanding is common in Cretaceous sandstones, consisting mainly of loose sand and weakly cemented sandstones. The numerical study was conducted based on the experimental laboratory data [17], where the particle size distribution (PSD) was taken from the field data [15,20,21].

In this work, we also focus on numerically exploring the correlation between the time-step of DEM and the time-step of CFD in a coupled system. The optimization of this relationship can result in a reduction of the CPU time for the sand production simulation of the oil and gas reservoir using CFD-DEM model.

2 Numerical Model Formulation

2.1 Model of the Particulate Phase

The discrete element method (DEM) is a computational model for examining the mechanical characteristics of discrete solid particles developed by Cundall and Strack [7]. The DEM technique is frequently used in a variety of scientific domains to look at how granular materials behave, including powders, soils, and rocks. The process replicates the motion and interactions of the particles under various circumstances depicting the particles as distinct and interacting objects. While Newton's second law governs the particle motion, the force-displacement relationships are used to calculate the contact forces between particles. We describe the translational and rotational motion of the particles by using the following equations:

$$m_i \frac{d\mathbf{v}_i}{dt} = \boldsymbol{f}_{pf,i} + \sum_{j=1}^{k_c} (\boldsymbol{f}_{c,ij} + \boldsymbol{f}_{damp,ij}) + m_i \boldsymbol{g} \tag{1}$$

$$I_i \frac{d\boldsymbol{\omega}_i}{dt} = \sum_{j=1}^{k_c} \boldsymbol{T}_{ij} \tag{2}$$

where m_i is the particle mass, $\mathbf{v_i}$ is the particle translational velocity, $\boldsymbol{\omega_i}$ is the particle angular velocity, I_i is the particle moment of inertia, k_c is the number of particles that interact with other particles, $\boldsymbol{f}_{pf,i}$ is the particle-fluid interaction force, $\boldsymbol{f}_{c,ij}$ and $\boldsymbol{f}_{damp,ij}$ are the contact force and damping force between particles, $\boldsymbol{T}_{ij}$ is the torque acting on particle i by particle j, and $m_i\boldsymbol{g}$ is the gravitational force.

The total particle-fluid interaction force $\boldsymbol{f}_{pf,i}$ acting on a single particle i can be defined as follows:

$$\boldsymbol{f}_{pf,i} = \boldsymbol{f}_{d,i} + \boldsymbol{f}_{\nabla p,i} + \boldsymbol{f}_{\nabla \cdot \boldsymbol{\tau},i} + \boldsymbol{f}_i^{''} \tag{3}$$

where $\boldsymbol{f}_{d,i}$ is the drag force, $\boldsymbol{f}_{\nabla p,i}$ is the pressure gradient force, $\boldsymbol{f}_{\nabla \cdot \boldsymbol{\tau},i}$ is the viscous force and $\boldsymbol{f}_i^{''}$ is the sum of other forces such as virtual mass force, Basset force, Saffman and Magnus lift forces [6].

The contact force $\boldsymbol{f}_{c,ij}$ between particle i and particle j is described by the linear spring-dashpot-slider model [7], which consists of normal (n) and tangential (t) components:

$$\boldsymbol{f}_{c,ij}^{(n)} = -k_n \boldsymbol{\delta}_{n,ij} - \eta_n \boldsymbol{v}_{n,ij} \tag{4}$$

$$\boldsymbol{f}_{c,ij}^{(t)} = -min\left(\mu \boldsymbol{f}_{c,ij}^{(n)}, k_t \boldsymbol{\delta}_{t,ij} + \eta_t \boldsymbol{v}_{t,ij}\right) \tag{5}$$

where $\boldsymbol{\delta_{ij}}$ and $\boldsymbol{v_{ij}}$ are the overlap and relative velocity between particle i and particle j, k is the spring stiffness constant, η is the dashpot damping coefficient, μ is the slider friction coefficient.

2.2 CFD-DEM Coupling

In CFD-DEM [24], the system of locally averaged Navier-Stokes equations are used to calculate the fluid flow in a porous medium. In so-called model A [28], only the porous fraction of the material is occupied by fluid, and the pressure drop is distributed between both the fluid and solid phases:

$$\begin{cases} \frac{\partial \alpha_f}{\partial t} + \nabla \cdot (\alpha_f \boldsymbol{u}) = 0 \\ \frac{\partial (\rho_f \alpha_f \boldsymbol{u})}{\partial t} + \nabla \cdot (\rho_f \alpha_f \boldsymbol{u}\boldsymbol{u}) = -\alpha_f \nabla p + \alpha_f \nabla \cdot \boldsymbol{\tau} + \rho_f \alpha_f \boldsymbol{g} + \boldsymbol{F}_{pf}^A \end{cases} \tag{6}$$

where ρ, $\boldsymbol{u}$, p are the density, dynamic velocity and pressure of fluid, α_f is the fluid volume fraction, $\boldsymbol{\tau} = \mu_f \left((\nabla \boldsymbol{u}) + (\nabla \boldsymbol{u})^T \right)$ is the stress tensor, where μ_f is the fluid dynamic viscosity, $\boldsymbol{F}_{pf}^A = \frac{1}{\Delta V} \sum_{i=1}^{n} (f_{d,i} + f_i'')$ is the volumetric particle-fluid interaction force in a single fluid cell of volume ΔV.

The drag force acting on an individual particle by fluid can be described by Di Felice correlation as follows [8]:

$$\boldsymbol{f}_{d,i} = \left(\frac{1}{8} C_{d,i} \rho_f \pi d_i^2 |\boldsymbol{u_i} - \mathbf{v_i}| (\boldsymbol{u_i} - \mathbf{v_i}) \right) \alpha_i^{2-\chi} \tag{7}$$

where $C_{d,i}$ is the drag coefficient, d_i is the diameter of a particle, $\boldsymbol{u_i}$ is the fluid velocity, $\mathbf{v_i}$ is the particle velocity, χ is the porosity correction factor, $\alpha_i = 1 - \sum_{i=1}^{n} V_{p,i} / \Delta V$ is the void fraction of a cell, where $V_{p,i}$ is the volume of a single particle.

We express the drag coefficient and porosity correction factor by the following empirical correlations:

$$C_{d,i} = \left(0.63 + \frac{4.8}{\sqrt{Re_i}} \right)^2 \tag{8}$$

$$\chi = 3.7 - 0.65 \exp \left(-\frac{(1.5 - \log_{10}(Re_i))^2}{2} \right) \tag{9}$$

where $Re_i = \frac{\rho_f d_i \alpha_i |\boldsymbol{u}_i - \mathbf{v_i}|}{\mu_f}$ is a particle Reynolds number.

2.3 Calculation of the Time-Step

The cfdemSolverPiso solver [16], which is based on Pressure-Implicit with Splitting of Operators (PISO) algorithm [11], solves the Navier-Stokes equations (Eq. 6) numerically with the finite volume method (FVM) taking into account the momentum exchange between fluid and solid phases. In the numerical schemes of the CFD-DEM coupled system, the time step is essential for the convergence of nonlinear problems. Therefore, the optimal time-step should be selected for both systems. In general, a smaller time-step outputs more accurate results, while a larger time-step leads to unstable and unrealistic results. There are two commonly used methodologies to compute the optimal time-step for DEM simulations: the time-step as a function of mass and stiffness [1] and the Rayleigh

time-step [18]. The time-step as a function of mass and stiffness is defined as follows:

$$\Delta t_{ms} \propto \sqrt{\frac{m}{k}} \tag{10}$$

where m and k are the mass and stiffness of a particle.

The Rayleigh time-step is expressed by the following equation:

$$\Delta t_R = \frac{\pi r}{\beta}\sqrt{\frac{\rho}{G}} \tag{11}$$

where r is the particle radius, ρ is the particle density, G is the particle shear modulus, and β is approximated by $\beta = 0.8766 + 0.163\nu$, where ν is the particle Poisson's ratio.

In CFD, the critical time-step can be determined by the Courant-Friedrichs-Lewy (CFL) condition [5]:

$$C = \Delta t \left(\sum_{i=1}^{n} \frac{u_i}{\Delta x_{cfd,i}} \right) \leq C_{max} \tag{12}$$

where C is the Courant number, Δt is the time-step of the CFD simulation, $\Delta x_{cfd,i}$ is the spacial size of a single fluid cell and n defines the number of spacial coordinates (typically, $n = 1$, 2 and 3). In general, C_{max} should be equal to 1 or less to ensure a stable simulation. It depends on the time-integration scheme of the solver. From the physical point of view, the CFL condition implies that the information (flow) should not travel over a single cell in one time-step.

In CFD-DEM coupling simulations, the DEM and CFD time-steps may run consecutive or concurrent regimes, see Fig. 1. In the consecutive regime, the data exchange between the DEM and CFD occurs after each other at the same core. In this case, all cores can be used at all times, which is optimal for effective resource usage. In the concurrent regime, the DEM and CFD calculations run in parallel for the space and occupy different cores at the same coupling time-step [16].

The accuracy and stability of CFD-DEM coupling simulations is determined by the time-step interval between those two distinct models. The relationship between DEM and CFD time-steps are defined by coupling number N, which is described by the following equation:

$$N = \frac{\Delta t_{CFD}}{\Delta t_{DEM}} \tag{13}$$

Typically, the DEM time-step is substantially shorter than the CFD time-step. There can be several DEM time-steps for a single CFD time-step. One can control the simulation time and improve the accuracy of the results by selecting the right value of N.

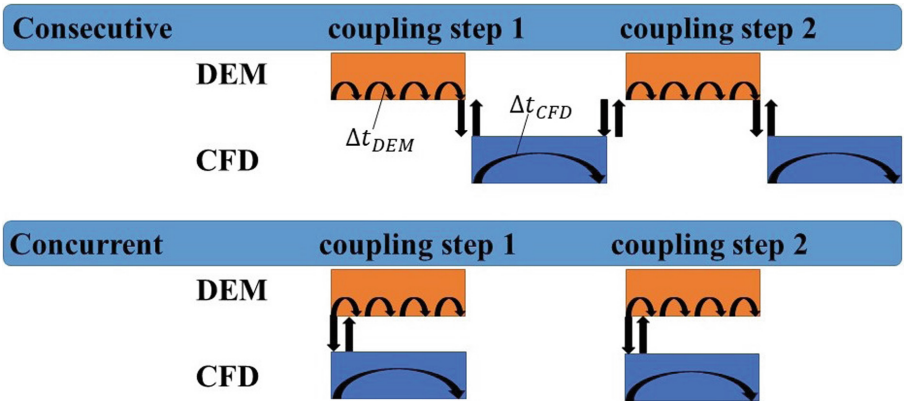

Fig. 1. The consecutive and concurrent time-step regimes in the CFD-DEM coupling (adapted from [16]).

3 Numerical Results

3.1 Numerical Setup of the Simulation

The optimal time-step size of the DEM and CFD ensures efficient and physically relevant simulation results. The DEM time-step size used in this simulation is equal to $\Delta t_{DEM} = 10^{-8}$ s and according to Eq. 11, it is 2.2% of Rayleight critical time-step, which is $\Delta t_R = 4.54 \cdot 10^{-8}$ s. In order to select an optimal coupling number for the CFD-DEM simulations, the following N coupling numbers are taken into consideration: 10, 100 and 1000. The results of those N numbers are compared with $N = 1$, where the DEM and CFD time-step values are the same. The optimal coupling number is selected by comparing the speedup and relative error of the sand production results. Based on those coupling numbers, the CFD simulations are configured with the following time-step values: $\Delta t_{CFD} = 10^{-7}$ s ($N = 10$), $\Delta t_{CFD} = 10^{-6}$ s ($N = 100$) and $\Delta t_{CFD} = 10^{-5}$ s ($N = 1000$), respectively. According to the CFL condition (Eq. 12), these CFD time-step values are within an acceptable range, since the maximum Courant number of $0.66 \cdot 10^{-6}$ is much less than 1.

In the sand production model, the numerical sample is initially prepared using only DEM modeling since it includes only a solid phase. The process is broken down into 3 distinct stages, namely: particle generation, compression and perforation. The particle generation involves creating new particles in the simulation environment and defining their shape and material properties. At the compression stage, the particles are compressed under a stress that corresponds to the experimental conditions. The numerical sample is then perforated vertically in the center. Afterwards, the sand production itself is modeled using CFD-DEM coupling, since it is a complex phenomenon that includes solid and fluid phases.

The coupling geometry is made up of two distinct DEM and CFD geometries, which should have the same size to ensure stable simulation. In the particle generation stage, the DEM geometry is constructed by 18 mm solid planes in a cuboid form, in which the spherical particles were initially created and contained for further simulation stages. The particle size distribution (PSD) and material parameters of the particles are provided in Table 1 and Table 2, respectively.

Table 1. Particle size distribution (PSD) of the simulated particles.

Mass fraction	0.058	0.075	0.088	0.1216	0.2264	0.1705	0.121	0.1395
Diameter, mm	0.3	0.36	0.4	0.44	0.5	0.55	0.6	0.71

Table 2. Material parameters of the simulated particles.

Parameter	
Density, kg/m^3	2605
Young's modulus, Pa	$2 \cdot 10^{10}$
Poisson's ratio	0.3
Restitution coefficient	0.8
Friction coefficient	0.2
Surface energy, J/m^2	60
Particle number	33 750

We use the same PSD and material characteristics as in works of [12,13] to supplement their investigations on the triaxial compression test and sand production phenomenon of unconsolidated reservoir sandstone using the coarse-graining methods in the modified JKR model [22]. This study focuses on the coarse-graining method for polydisperse particles with coarse-graining factor (k_{cg}) of 2. The initial particle size is doubled and the material properties of the particles are scaled accordingly. Therefore, the modeling applied with coarse-graining methods is also accelerated.

In the compression stage, a stress of 1 MPa, which is applied from the top plate to compress the particles in the cell, maintains the porosity of the sample at 42%. After the compression, the modified JKR is applied to create the bonds between particles. The numerical sample is then perforated in the center with a penetrometer, which results in breaking the bonds in perforation locations. After removing the penetrometer from the sample, we initiate the sand production process with the fluid injection by simulating the CFD-DEM coupling. The hole size for the sand production in the DEM model equals to 2.8 mm.

The geometry of the coupling is illustrated in Fig. 2a. The numerical sample size has length of L = 18 mm and height h = 8.82 mm. The CFD domain is segmented into 12x12x6 cells in xyz directions. The particles are considerably

smaller than the dimensions of a single CFD cell, which is capable of accommodating several particles. Hence, the size of the cell in all three directions meets the criteria for the unresolved case, as per the equation below [4]:

$$\frac{\Delta x_{cfd}}{\bar{d}_p} > 3 \tag{14}$$

where $\bar{d}_p$ is the particle average diameter.

The boundary conditions of the model are demonstrated in Fig. 2b. The fluid with velocity of 10^{-4} m/s is injected from two planes which are normal to y-axis (green color). The rest of the planes are set to cyclic boundary conditions (gray color). The pressure exerted on the top and bottom holes is equal to atmospheric pressure (red color). The initial conditions of the model are as follows: $U(0) = 0$ and $P(0) = 0$. The CFD-DEM simulations were performed using the CFDEM coupling tool [9], which integrates the DEM commercial software (Aspherix 6.0) [16] and the CFD open-source software OpenFOAM [3]. The simulations were executed on the high-performance computing (HPC) system equipped with an Intel(R) Xeon(R) Gold 6230R CPU @ 2.10 GHz containing 52 cores. Each case of the coupling number is simulated using 4 cores with parallel computing in 4x1x1 decomposition along the x, y and z axes.

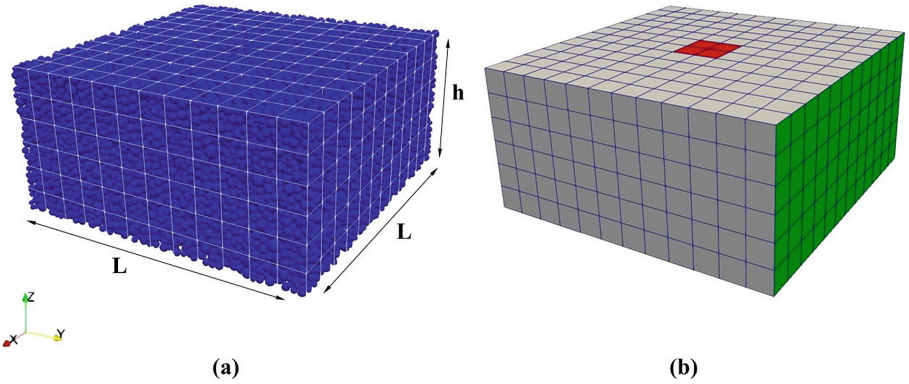

Fig. 2. (a) Geometry and (b) boundary conditions of the model. P = const is in the red zone, U = const is in the green zone, and periodic boundaries is in the grey zone. (Color figure online)

3.2 Analysis of Time-Step

The simulation time for all cases is 0.04 s, in which the sand production become in transient behavior. Figure 3 shows the snapshots of the flow streamlines with fluid velocity in the background and particle velocity in the numerical sample at 0.005 s, 0.02 s, and 0.04 s from the initial condition. At the beginning, we observe an increased fluid velocity at the perforation locations, which leads to

intense mobilization of sand towards the top hole. At t = 0.02 s, the velocity of the fluid decreases significantly, resulting in a deceleration of the sand production rate. At the final time ($t = 0.04$ s), the fluid flow reaches a stationary flow condition, with streamlines being uniformly distributed throughout the sample. As a consequence, there is no occurrence of sand production at this time.

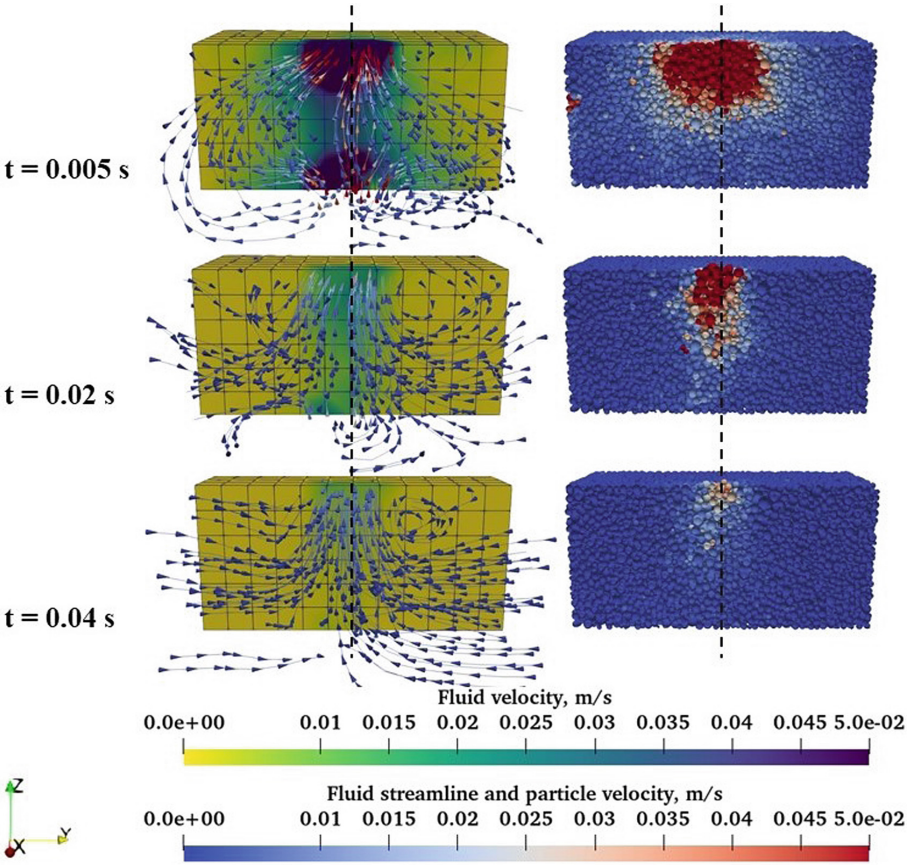

Fig. 3. Flow streamlines with the fluid velocity background and particle velocity.

Figure 4 demonstrates the comparison of cumulative sand production at $N = 1$, 10, 100 and 1000 cases. During the intensive sand production, which is continued from the beginning until 0.005 s, almost a similar amount of sand is produced in all cases. However, in the ranges of gradual (0.005 s–0.02 s) and transient (0.02 s–0.04 s) sand production, the curves become slight different. For instance, the most difference is observed when the simulations are performed at $N = 1000$ coupling number. In that case, we observe an increase in cumulative sand production in the gradual regime, and a decrease in the transient behavior

compared to $N = 1$ coupling number. Although the sand production of $N = 10$ and $N = 100$ is slightly less than $N = 1$, the curves of those coupling numbers are in a similar pattern. The most excellent results are observed at $N = 100$, where the sand production rate and curve pattern are relatively similar to $N = 1$ throughout the entire simulation time.

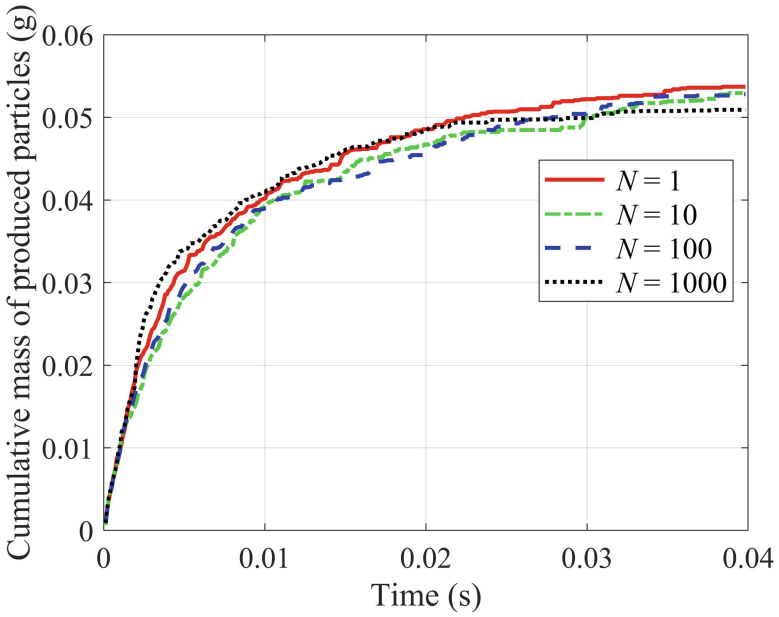

Fig. 4. Comparison of cumulative sand production at $N = 1$, 10, 100 and 1000.

The effect of the coupling numbers on bonding behavior of the particles can be better understood by comparing the bond number and bond ratio in the sample. The cementation of the numerical sample is represented by utilizing the modified JKR contact model [22], in which the particles are cohesively bonded to each other. The bond number shows all existing bonds between particles in the sample. It is possible that the particles might be in contact with other particles, but are not bonded. This usually occurs when the bonds are broken by a force acting on the sample. Particles that are not bonded to each other are modeled by the Hertz contact model [10]. The bond ratio describes the ratio of the bonded particle number to the total number of contacts in the sample. Figure 5a demonstrates the total number of bonds that exist between particles of the coupling numbers $N = 1$, $N = 10$, $N = 100$ and $N = 1000$. At the initial condition all cases have $1.34 \cdot 10^5$ bonds in total. In the intensive sand production regime, the bonds reduced dramatically. As flow becomes stationary, no new breakage of bonds occurs in the sample. The bond numbers of N =10 and $N = 100$ show similar pattern throughout the simulation finishing at about

$1.21 \cdot 10^5$ bonds. This is just above the $N = 1$ results, which bond number equals to $1.206 \cdot 10^5$ at the final time. The $N = 1000$ case loses a drastic number of bonds with intensive sand production and reaches $1.192 \cdot 10^5$ bonds at the end. Figure 5b shows the bond ratio in the sample of the coupling numbers $N = 1$, $N = 10$, $N = 100$ and $N = 1000$. We observe a sharp decrease on all bond ratio cases during the intensive sand production. As production becomes in transient regime, the bond ratios increase gradually. These results demonstrate that the bond ratio of the $N = 100$ coupling number is more accurate compared to others and behave in similar pattern with $N = 1$ case.

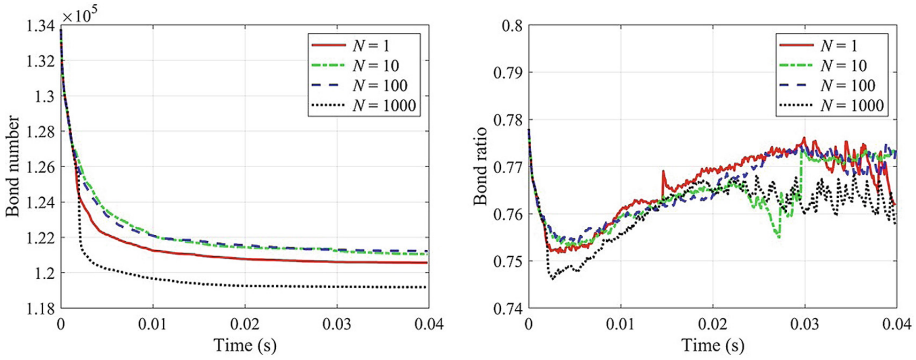

Fig. 5. (a) Bond number and (b) bond ratio of the particles at $N = 1$, 10, 100 and 1000.

We evaluate the CPU time, speedup and root mean squared relative error (RMSRE) to compare the sand production modelling results at different coupling numbers (see Table 3). To examine the accuracy of the simulation results, the RMSRE is given as follows:

$$RMSRE = \sqrt{\frac{1}{n}\sum_{i=1}^{n}\left|\frac{M^i_{d,N=1} - M^i_{d,N_{coupling}}}{M^i_{d,N=1}}\right|^2} \times 100 \tag{15}$$

where $M^i_{d,N=1}$ is the i-th dimensionless cumulative sand production at $N = 1$ and $M^i_{d,N_{coupling}}$ is the i-th dimensionless cumulative sand production at other coupling numbers.

According to Table 3, the reference coupling number $N = 1$ demonstrates the longest CPU time of 6665 min. The coupling numbers $N = 100$ and $N = 1000$ significantly accelerate the simulation by 8.8 and 9.52 times compared to $N = 10$, which exhibits a speedup of 5.98. These results show that the CPU time of the modeling process is greatly reduced when the coupling number is increased to $N = 1000$. However, this enhancement in efficiency came at the expense of lower

accuracy, as specified by an elevated root mean square relative error (RMSRE) of 5.19% in the total sand production at t = 0.04 s. On the other hand, simulations with coupling numbers $N = 10$ and $N = 100$ provide more acceptable RMSRE values of 1.42% and 1.67% at t = 0.04 s, respectively. Throughout the entire simulation, the coupling numbers $N = 100$ and $N = 1000$ with RMSREs of 4.9% are more accurate than $N = 10$ (RMSRE = 6.05%). In terms of bonding behavior, the $N = 10$ and $N = 100$ coupling numbers demonstrate reasonable results with RMSRE values of 0.68% and 0.65% in bond number, 0.69% and 0.39% in bond ratio, respectively. In contrast, the $N = 1000$ is less accurate with RMSRE of 1.27% in bond number and 0.8% in bond ratio. These findings suggest that a considerable increase in coupling number can improve the computational efficiency, but can also reduce the accuracy of the model.

Table 3. CPU time, speedup and root mean squared relative error (RMSRE) of the sand production simulations at $N = 1$, 10, 100 and 1000 coupling numbers.

Coupling number	CPU time, min	Speedup	RMSRE, %			
			Sand production	Sand production (at t = 0.04 s)	Bond number	Bond ratio
1	6665	1	0	0	0	0
10	1113	5.98	6.05	1.42	0.68	0.69
100	757	8.8	4.9	1.67	0.65	0.39
1000	700	9.52	4.9	5.19	1.27	0.8

4 Conclusion

The main objective of this study is to explore the optimal coupling number of CFD-DEM modeling to ensure physically stable, accurate and efficient results. Specifically, we use the modified JKR contact model to investigate sand production phenomenon in unconsolidated reservoirs, with the particle size distribution and material characteristics being associated with the Kazakhstan reservoir sample. The following coupling numbers $N = 10$, $N = 100$ and $N = 1000$ are taken into account to choose the suitable coupling number for the CFD-DEM simulations. The results are compared with those of $N = 1$, in which the DEM and CFD time-step values are identical. Initially, we provide the snapshots of the flow streamlines, fluid and particle velocities to demonstrate the transient behavior of the sand production. Then, the CPU time, speedup and root mean squared relative error of the sand production results at different coupling numbers are compared. In all cases, the CPU time is significantly reduced compared to $N = 1$. Particularly, the fastest calculations are observed at $N = 100$ and $N = 1000$, in which the speedup is 8.8 and 9.52, respectively. Most of the results show that N=10 and $N = 100$ coupling numbers demonstrate more accurate results compared to the $N = 1000$. Especially, this tendency can be seen from the final sand

production and bonding behavior results. Based on these findings, we consider that the $N = 10$ and $N = 100$ are optimal coupling numbers for the sand production modeling to ensure physically relevant simulations with high accuracy and sufficient acceleration.

Acknowledgements. The authors wish to acknowledge the support of the research grant, no. AP19575428, from the Ministry of Science and Higher Education of the Republic of Kazakhstan. Authors gratefully acknowledge the support of the Nazarbayev University Faculty Development Competitive Research Grant (NUFDCRG), Grant No. 20122022FD4141.

References

1. Belytschko, T.: An overview of semidiscretization and time integration procedures. Computational Methods for Transient Analysis (A 84-29160 12-64), pp. 1–65. North-Holland, Amsterdam (1983)
2. Blais, B., Lassaigne, M., Goniva, C., Fradette, L., Bertrand, F.: Development of an unresolved CFD-DEM model for the flow of viscous suspensions and its application to solid-liquid mixing. J. Comput. Phys. **318**, 201–221 (2016)
3. Chen, G., Xiong, Q., Morris, P.J., Paterson, E.G., Sergeev, A., Wang, Y.: OpenFOAM for computational fluid dynamics. Not. AMS **61**(4), 354–363 (2014)
4. Clarke, D.A., Sederman, A.J., Gladden, L.F., Holland, D.J.: Investigation of void fraction schemes for use with CFD-DEM simulations of fluidized beds. Ind. Eng. Chem. Res. **57**(8), 3002–3013 (2018)
5. Courant, R., Friedrichs, K., Lewy, H.: Über die partiellen differenzengleichungen der mathematischen physik. Math. Ann. **100**(1), 32–74 (1928)
6. Crowe, C.T., Schwarzkopf, J.D., Sommerfeld, M., Tsuji, Y.: Multiphase Flows with Droplets and Particles. CRC Press, Boca Raton (2011)
7. Cundall, P.A., Strack, O.D.: A discrete numerical model for granular assemblies. geotechnique **29**(1), 47–65 (1979)
8. Di Felice, R.: The voidage function for fluid-particle interaction systems. Int. J. Multiph. Flow **20**(1), 153–159 (1994)
9. Goniva, C., Kloss, C., Deen, N.G., Kuipers, J.A., Pirker, S.: Influence of rolling friction on single spout fluidized bed simulation. Particuology **10**(5), 582–591 (2012)
10. Hertz, H.: Ueber die berührung fester elastischer körper (1882)
11. Issa, R.I.: Solution of the implicitly discretised fluid flow equations by operator-splitting. J. Comput. Phys. **62**(1), 40–65 (1986)
12. Kazidenov, D., Khamitov, F., Amanbek, Y.: Coarse-graining methods for the modified jkr contact model on a triaxial compression test. In: 56th US Rock Mechanics/Geomechanics Symposium. OnePetro (2022)
13. Kazidenov, D., Khamitov, F., Amanbek, Y.: Coarse-graining of CFD-DEM for simulation of sand production in the modified cohesive contact model. Gas Sci. Eng. **113**, 204976 (2023)
14. Kazidenov, D., Omirbekov, S., Zhanabayeva, M., Amanbek, Y.: Experimental and numerical study of the effect of polymer flooding on sand production in poorly consolidated porous media. Preprint (2023)
15. Khamitov, F., Minh, N.H., Zhao, Y.: Numerical investigation of sand production mechanisms in weak sandstone formations with various reservoir fluids. Int. J. Rock Mech. Min. Sci. **154**, 105096 (2022)

16. Kloss, C., Goniva, C., Hager, A., Amberger, S., Pirker, S.: Models, algorithms and validation for opensource DEM and CFD-DEM. Prog. Comput. Fluid Dyn. Int. J. **12**(2–3), 140–152 (2012)
17. Kozhagulova, A., Minh, N.H., Zhao, Y., Fok, S.C.: Experimental and analytical investigation of sand production in weak formations for multiple well shut-ins. J. Petrol. Sci. Eng. **195**, 107628 (2020)
18. Li, Y., Xu, Y., Thornton, C.: A comparison of discrete element simulations and experiments for sandpiles composed of spherical particles. Powder Technol. **160**(3), 219–228 (2005)
19. Norouzi, H.R., Zarghami, R., Sotudeh-Gharebagh, R., Mostoufi, N.: Coupled CFD-DEM Modeling: Formulation, Implementation and Application to Multiphase Flows. Wiley, Hoboken (2016)
20. Rakhimzhanova, A., Thornton, C., Amanbek, Y., Zhao, Y.: Numerical simulations of cone penetration in cemented sandstone. In: EPJ Web of Conferences, vol. 249, p. 14010. EDP Sciences (2021)
21. Rakhimzhanova, A., Thornton, C., Amanbek, Y., Zhao, Y.: Numerical simulations of sand production in oil wells using the CFD-DEM-IBM approach. J. Petrol. Sci. Eng. **208**, 109529 (2022)
22. Rakhimzhanova, A.K., Thornton, C., Minh, N.H., Fok, S.C., Zhao, Y.: Numerical simulations of triaxial compression tests of cemented sandstone. Comput. Geotech. **113**, 103068 (2019)
23. Sun, Z., Balhoff, M.T., Espinoza, D.N.: Fluid injection induced fracture initiation based on a resolved CFD-DEM approach. In: 52nd US Rock Mechanics/Geomechanics Symposium. OnePetro (2018)
24. Tsuji, Y., Kawaguchi, T., Tanaka, T.: Discrete particle simulation of two-dimensional fluidized bed. Powder Technol. **77**(1), 79–87 (1993)
25. Versteeg, H.K., Malalasekera, W.: An Introduction to Computational Fluid Dynamics: The Finite Volume Method. Pearson Education, London (2007)
26. Wang, X., Gong, L., Li, Y., Yao, J.: Developments and applications of the CFD-DEM method in particle-fluid numerical simulation in petroleum engineering: a review. Appl. Therm. Eng. 119865 (2022)
27. Willson, S., Moschovidis, Z., Cameron, J., Palmer, I.: New model for predicting the rate of sand production. In: SPE/ISRM rock mechanics conference. OnePetro (2002)
28. Zhu, H., Zhou, Z., Yang, R., Yu, A.: Discrete particle simulation of particulate systems: theoretical developments. Chem. Eng. Sci. **62**(13), 3378–3396 (2007)